The SARS-CoV-2 Transcriptional Metabolic Signature in Lung Epithelium

Avner Ehrlich[1,2,*], Skyler Uhl[3,*], Konstantinos Ioannidis[1,2], Matan Hofree[5], Benjamin R. tenOever[3], Yaakov Nahmias[1,2,#]

1. Grass Center for Bioengineering, Benin School of Computer Science and Engineering, Jerusalem, Israel.
2. Department of Cell and Developmental Biology, Silberman Institute of Life Sciences, Jerusalem, Israel
3. Department of Microbiology, Icahn School of Medicine at Mount Sinai, New York, USA
4. Klarman Cell Observatory, The Broad Institute of Harvard and MIT, Cambridge, MA

* Marks equal contribution
# Correspondence: ynahmias@cs.huji.ac.il

Abstract

Viruses are efficient metabolic engineers that actively rewire host metabolic pathways to support their lifecycle. Charting SARS-CoV-2 induced metabolic changes in lung cells could offer insight into COVID-19 pathogenesis while presenting new therapeutic targets. Here we show that the transcriptional response SARS-CoV-2 in primary lung epithelial cells and biopsies of COVID-19 patients is predominantly metabolic. This transcriptional signature was dominated by changes to lipid metabolism and the induction of IRE1 and PKR pathways of endoplasmic stress in a process regulated by several viral proteins. Transcriptional regulatory analysis of these changes reveals small clusters of transcription factors modulating key enzymes in each pathway. The upregulation of glycolysis and the dysregulation of the citric acid cycle was mediated by NFκB and RELA. While the upregulation of fatty acid and cholesterol synthesis showed a more complex control conditionally modulated by ER-stress activated PPARγ, C/EBP, and PPARα. Viral protein ORF3a appeared to interact with all three pathways suggesting both direct and indirect modulation of host metabolism. Finally, we show that PPARα-agonist fenofibrate reversed the metabolic changes induced by SARS-CoV-2 blocking viral replication. Taken together, our data suggest that elevated lipid metabolism may underlie aspects of COVID-19 pathogenesis, offering new therapeutic avenues in targeting this critical pathway on which the virus relies.

Introduction

The severe acute respiratory syndrome coronavirus 2 (SARS-CoV-2) is a positive-strand RNA virus of the *sarbecovirus subgenus* that is related to SARS. The virus is expected to infect over 40% of the world population and causes pulmonary disease, termed COVID-19, in 5% to 20% of those infected. Like other viruses, SARS-CoV-2 must rely on host machinery to propagate, rewiring cellular metabolism to generate macromolecules needed for virion replication, assembly, and egress. Elucidating the metabolic response to SARS-CoV-2 infection could provide insight into the pathogenesis of COVID-19 and suggest new therapeutic avenues to combat the disease.

Recent work suggests that COVID-19 progression is dependent on metabolic mechanisms. Elevated blood glucose and lipid levels were found to be risk factors for SARS-CoV-2 induced acute respiratory distress, independently from diabetes (Bornstein et al., 2020; Zhu et al., 2020). This data correlates with reports that the SARS virus caused insulin resistance in 50% of the patients over the course of infection (Yang et al., 2010). In fact, SARS infection results in hyperlipidemia and hyperglycemia in patients even 12 years post-recovery (Wu et al., 2017). Indeed, palmitoylation of SARS spike proteins was shown to be essential for virion assembly (McBride and Machamer, 2010), while other coronaviruses showed elevated lipid accumulation upon infection (Yan et al., 2019b; Yuan et al., 2019). These data suggest that

metabolic alterations may play a significant role in the lifecycle of SARS-CoV-2 and the progression of COVID-19.

In this work we studied the metabolic rewiring induced by SARS-CoV-2 infection in the transcriptional signature of primary bronchial epithelial cells, validating our results in lung biopsy samples of COVID-19 patients. Our data show a significant metabolic response in SARS-CoV-2 infected lungs covering 60% of the differentially expressed genes. This transcriptional signature was dominated by changes to lipid metabolism and the induction of IRE1 and PKR pathways of endoplasmic stress in a process that appeared to be tightly regulated by multiple viral proteins. Transcriptional regulatory analysis of these changes reveals small clusters of transcription factors modulating key enzymes in each pathway. The upregulation of glycolysis and the dysregulation of the citric acid cycle was mediated by NFκB and RELA. While the upregulation of fatty acid and cholesterol synthesis showed a more complex control conditionally modulated by ER-stress activated PPARγ, C/EBP, and PPARα inhibition. Viral protein ORF3a appeared to interact with all three pathways suggesting both direct and indirect modulation of host lipid and glucose metabolism. Finally, we show that PPARα-agonist fenofibrate reversed the metabolic changes induced by SARS-CoV-2, blocking viral production. Our results suggest that FDA-approved drugs such as fenofibrate or cloperastine could directly target host metabolic pathways to minimize virus replication and perhaps suppress its pathogenesis in lung tissue.

Results

The metabolic fingerprint of SARS-CoV-2 infection

Primary human bronchial epithelial cells were infected with SARS-CoV-2 at a MOI of 2. Infected cells became noticeably smaller, showing vacuolization. RNA-Seq analysis of infected primary cells identified 535 differentially expressed genes (FDR<0.05). Enrichment analysis identified the regulation of viral transcription (FDR<$3x10^{-2}$), immune processes (FDR<$9x10^{-4}$), cellular response to stress (FDR<$5x10^{-11}$), and inflammation (FDR<$3x10^{-3}$). Similar RNA-Seq analysis was carried out on lung biopsies taken from COVID-19 and uninfected patients identifying 2,353 differentially expressed genes and similar enrichments (**Fig. 1A**; **Supplement Table S1**).

Interestingly, both experiments showed enrichment of metabolic processes (FDR<$4x10^{-4}$), particularly lipid and carbohydrate metabolic processes (**Fig. 1A**). Our analysis revealed that 59% to 65% of the differentially expressed genes are metabolism-related, with 8% to 18% of the genes associated with lipid metabolism (**Fig. 1B**). We have previously shown that classical annotations are poorly suited to investigate metabolic pathways in viral infection (Levy et al., 2016). Thus, we aggregated metabolic categories to form a wider aspect of several canonical pathways (**Supplement Table S2**). Our metabolism-focused analysis shows significant SARS-CoV-2-induced enrichment of lipid metabolism (FDR<$3x10^{-17}$), mitochondrial function (FDR<$7x10^{-4}$), and glucose metabolism (FDR<$2x10^{-2}$) in both SARS-CoV-2-infected primary cultures and patient biopsies (**Fig. 1C**). In contrast, changes in amino acid metabolism were not significant.

These transcriptional changes suggest a transformation of the metabolic landscape of primary lung epithelium by SARS-CoV-2 infection. Glycolysis is upregulated, providing nucleotides for viral replication (Mayer et al., 2019), while the upregulation of lipogenesis supports lipid rafts and palmitoylation of viral proteins, essential components of the viral replication complex (Yan et al., 2019b) (**Fig. 1D**). Other cellular processes (blue arrows) are superimposed on the

metabolic analysis (**Fig. 1D**). The upregulation of endoplasmic stress due to viral replication appears to be associated with lipid accumulation and oxidative stress due to mitochondrial dysfunction (**Fig. 1D**).

SARS-CoV-2 induced endoplasmic stress

RNA-Seq analysis showed a significant cellular response to stress (FDR<$5x10^{-11}$), particularly genes associated with endoplasmic reticulum (ER) stress (**Fig. 2A**). Infection induced the dsRNA-activated protein kinase R (PKR) pathway leading to differential expression of downstream ATF4 in both primary cells and patient biopsies (**Supplement Fig. S1**). IRE1 pathway was similarly activated, leading to increased splicing of XBP1 and activation of PPARγ and C/EBP. In contrast, both ATF6 and PERK pathways of ER stress were downregulated, suggesting direct modulation of endoplasmic stress pathways by the virus.

Recently, Gordon and colleagues identified human proteins physically interacting with SARS-CoV-2 proteins(Gordon et al., 2020). Examining the viral-host protein-protein interactions from this study, we charted the physical interactions of viral proteins with each of the ER stress pathways (**Fig. 2B**; **Supplement Fig. S1**). Our analysis reveals a significant association of viral proteins with key regulators in each pathway. Importantly, while the IRE1 pathway appeared to be upregulated, JNK was bound by no less than 6 viral proteins, its expression downregulated by infection (**Fig. 2B**). Similarly, while PKR activation by viral RNA led to ATF4 activation, the PP1 negative feedback loop was downregulated and bound by 5 different viral proteins (**Fig. 2B**).

SARS-CoV-2 infection up-regulates lipogenesis

Lipid accumulation is often driven by endoplasmic stress (Han and Kaufman, 2016) and can support the viral lifecycle through increased palmitoylation and lipid rafts, two essential components of the viral replication complex (Takahashi and Suzuki, 2011). Indeed, SARS-CoV-2 infection shows the upregulation of lipogenesis and cholesterol synthesis genes in primary bronchial epithelial cells (**Fig. 2C**). The Infection differentially up-regulates both HMG-CoA synthase (HMGCS) and Squalene monooxygenase (SQLE) rate-limiting steps in cholesterol synthesis. Fluorescence microscopy confirmed a significant perinuclear accumulation of neutral lipids ($p<0.01$) and phospholipids ($p<0.05$) in SARS-CoV-2 infected cells (**Fig. 2D**).

A genome-wide search for transcriptional regulators of lipid metabolism (**Supplementary Table S3-4**) showed that SARS-CoV-2 infection activated a cluster of interconnected transcription factors including NFκB, RELA, C/EBP, and lipid-activated nuclear receptors PPARα and PPARγ (**Fig. 2E**). Regulatory analysis of COVID-19 biopsy data confirmed the activation of NFκB, RELA, C/EBP, PPARα and PPARγ validating our results (**Fig. 2E**). Charting the physical interactions of viral proteins(Gordon et al., 2020) with the lipogenesis pathway and its regulators reveals a putative connection of viral proteins M and ORF9c to key lipogenesis enzymes (**Fig. 2F**). Viral proteins M, NSP7, and NSP12 also interact with the key transcription factors regulating lipid metabolism, while NSP5, ORF3a, and NSP12 interacted with NFκB and RelA through HDAC2, HMOX1, and RIPK1 (**Fig. 2F**). To validate these interactions, we expressed individual viral protein in primary bronchial epithelial cells and studied their intracellular lipids using fluorescence microscopy (**Fig. 2G**). Expression of NSP5 and ORF3a results in an 80% and 50% increase in intracellular phospholipids ($p<0.05$). These results suggest that viral protein regulation of NFκB and RelA plays a role in SARS-CoV-2 modulation of lipid metabolism.

Evidence of SARS-CoV-2 induced mitochondrial stress

Coronavirus infection is thought to be associated with mitochondrial stress (Latif Reshi, 2018; Shi et al., 2019) which commonly results in increased reliance on anaerobic glycolysis as part of a viral-induced *Warburg effect (Levy et al., 2016)*. Enrichment analysis showed that SARS-CoV-2 differentially regulated genes related to the mitochondria (FDR<$7x10^{-4}$) and the cellular response to oxidative stress (FDR<$3x10^{-5}$). Indeed, SARS-CoV-2 infection downregulated genes of the citric acid cycle, while upregulating ATP citrate lyase (ACLY) an important step in fatty acid biosynthesis, directing resources away from oxidative phosphorylation (**Fig. 3A**). Examining the transcriptional regulators of mitochondrial function showed that SARS-CoV-2 infection activated a cluster of interconnected transcription factors including RELA and NFκB as well as SP1 and JUN (**Fig. 3B**). Regulatory analysis of COVID-19 biopsy data confirmed the activation of RELA, NFκB, SP1, and JUN factors implicated in the response to mitochondrial stress (Son et al., 2010) (**Fig. 3B**). Analysis of SARS-CoV-2 proteins showed potential physical interactions between multiple viral proteins and enzymes of the citric acid cycle, as well as NFκB and RelA (**Fig. 3C**).

To validate viral protein interactions in this pathway, we analyzed the mitochondrial membrane potential (ΔΨm) of primary lung cells expressing individual viral proteins (**Fig. 3D**). Expression of ORF3a caused a significant 45% decrease in the mitochondrial membrane potential ($p<0.001$). Analysis of respiratory activity showed a significant decrease in mitochondrial capacity of primary bronchial epithelial cells expressing NSP12, ORF6, ORF3a, and N ($p<0.001$; **Fig. 3E**). These results confirm the role of ORF3a and to some extent, NSP12 and N in SARS-CoV-2 induced mitochondrial stress.

SARS-CoV-2 infection induces anaerobic glycolysis through NFκB and RelA

We have previously shown that HCV replication was dependent on the upregulation of glycolysis, while others showed a similar relationship in influenza and rhinovirus infections (Gualdoni et al., 2018; Kilbourne, 1959; Levy et al., 2016). SARS-CoV-2 infection shows a similar upregulation of key glycolysis genes (**Fig. 3F**) including hexokinase 2 (HK2) and pyruvate kinase isozyme (PKM), both key rate-limiting enzymes in anaerobic glycolysis. This signature, together with downregulation of respiration, demonstrates a virus-induced *Warburg effect*, which would be difficult to identify in immortalized cells due to their reliance on anaerobic glycolysis.

A search for transcriptional regulators of glucose metabolism showed the involvement of NFκB and RelA (**Fig. 3G**), transcription factors recently implicated in the metabolic adaptation of mature cells to anaerobic glycolysis (Zhao et al., 2020). Regulatory analysis of COVID-19 biopsy data confirmed the activation of NFκB, RelA, and to a lesser extent SP1 (**Fig. 3G**). Metabolic analysis of SARS-CoV-2 infected lung cells showed a 50% increase ($p<0.001$) in lactate production (**Fig. 3H**), shifting the lactate over glucose ratio from 1 to 1.7 (**Supplement Fig. S2**) indicating a shift to glycolytic phenotype. Analysis of fluorescent glucose analog, 2-NDBG, uptake confirmed a marked increase in intracellular glucose in SARS-CoV-2 infected cells (**Fig. 3I**).

Network integration analysis reveals a putative connection NSP7 and ORF8 to key glycolytic enzymes through POFUT1 and CYB5R3 (**Fig. 3J**). To validate these interactions, we analyzed the metabolism of primary cells expressing viral proteins (**Fig. E**). Expression of NSP5, ORF8, or M increased the extracellular acidification rate by 28 to 68% indicating a shift to glycolysis. Glutamine uptake was reduced by 20% (data not shown). Taken together these results suggest both direct and transcriptional modulation of glucose metabolism by SARS-CoV-2 infection.

Emerging therapeutic targets of SARS-CoV-2 induced host metabolic pathways

The metabolic pathways changed by SARS-CoV-2 offer several opportunities to interfere with the virus lifecycle (**Fig. 4A-B**). Inhibiting glycolysis was previously shown to block viral replication(Gualdoni et al., 2018; Kilbourne, 1959; Levy et al., 2016). Glucose transport inhibitors are particularly effective in patients. Recent work identified cloperastine (Hustazol®) a clinically approved cough suppressant as an SGLT1 inhibitor (Oranje et al., 2019) suggesting it could effectively limit glycolysis in lung cells. Blocking of fatty acid and cholesterol synthesis through PPARα activation and HMGCR inhibition, using bezafibrate (Bezalip®) and simvastatin (Zocor®) respectively were shown to be effective in inhibiting HCV replication (Fujita et al., 2006; Ikeda et al., 2006). A similar reliance on these pathways in SARS-CoV-2 infection could lead to a similar antiviral effect.

To validate these metabolic targets, we treated SARS-CoV-2 infected lung cells with drugs that target lipid, glucose, and mitochondrial metabolism (**Fig. 4C-F**). GW9662 a small molecule inhibitor of PPARγ blocked neutral and phospholipid accumulation ($p<0.01$) and reduced viral load by 2-folds, but also affected cell viability (**Fig. 4D-E**; **Supplement Fig. S3**). Cloperastine (Hustazol®) recently identified as an SGLT1 inhibitor (Burggraaff et al., 2019), also reduced viral load by 3-fold ($p<0.01$) but without affecting cell viability (**Supplement Fig. S3)**. In contrast, the PPARα agonist fenofibrate (Tricor®) blocked phospholipid accumulation ($p<0.001$) and as well as the increase in glycolysis (**Fig. 4D-E**). A 5-day treatment with fenofibrate reduced viral load by 2-logs ($p<0.001$) without affecting cell viability (**Fig. 4F**, **Supplement Fig. S3**). These results suggest that lipid metabolism is an important pathway for SARS-CoV-2 replication and a promising therapeutic target.

Discussion

Viruses, like SARS-CoV-2, depend on host cells to obtain macromolecules essential for their lifecycle. Glycolysis is often upregulated to supply the virus with nucleotides through the pentose phosphate pathway. Both rhinovirus and influenza A virus increase glycolysis within minutes of infection through non-transcriptional mechanisms, while the hepatitis c virus (HCV) upregulated glycolysis only days post-infection through HNF4α (Gualdoni et al., 2018; Levy et al., 2016; Smallwood et al., 2017). Like HCV infection, SARS-CoV-2 induction of glycolysis appears to be transcriptionally mediated by upregulation of NFκB and RELA, inflammatory transcription factors recently implicated in the metabolic adaptation of mature cells to anaerobic glycolysis (Zhao et al., 2020). This activation of the NFκB pathway independent of the canonical pathogen-associated molecular patterns may also explain how infection results in such high levels of chemokines despite very low levels of Type I and III interferons (Blanco-Melo et al., 2020).

Viral infections are often associated with the induction of mitochondrial stress through direct or indirect mechanisms. SARS coronavirus ORF8b aggregates were shown to induce ER stress and mitochondrial dysfunction (Shi et al., 2019), while influenza protein PB1-F2 specifically localized to the mitochondrial membrane causing dysfunction (Yoshizumi et al., 2014). Several SARS-CoV-2 proteins were found to bind mitochondrial host proteins (Gordon et al., 2020), and our data suggest that ORF3a may be directly responsible for mitochondrial stress (**Fig. 3**). The physical interactions of ORF3a with both NFκB and RELA appear to three metabolic pathways (**Fig. 2-3**) and its expression in primary cells leads to coordinated metabolic changes as the cells shift from mitochondrial respiration to lipid accumulation.

Cellular response to stress (GO:0033554) is the single most prominent transcriptional response to SARS-CoV-2 infection, dominated by the induction of ER stress. The induction of dsRNA-activated PKR pathway is not surprising in cells infected with RNA viruses. Influenza A virus similarly induces pathways of ER stress, including IRE1α to support increased viral replication and infectivity (Hassan et al., 2012). SARS, on the other hand, activates the PERK pathway inducing autophagy through the cAMP response element (Fung and Liu, 2019). Here, we show that SARS-CoV-2 induces the PKR and IRE1α pathways but not PERK or ATF6 (**Fig. 2A**). IRE1α splicing of XBP1 leads to activation of C/EBP and PPARγ whose target genes are upregulated in lipid metabolism (**Fig. 2C-E**), while JNK EDEM inhibition prevents the non-specific ER-associated degradation process. Network integration analysis reveals numerous physical interactions between SARS-CoV-2 viral proteins at key decision points, which might suppress JNK, SPP1, and SP1 to direct ER stress pathways toward lipogenesis rather than apoptosis.

SARS-CoV-2 induction of ER stress appears to upregulate fatty acid and cholesterol synthesis in lung epithelial cells (**Fig. 2C-D**). Genes involved in palmitoylation such as IFITM1/3 are differentially expressed (**Fig. 1**) permitting the efficient modification of the coronavirus spike protein. Cholesterol synthesis pathway genes including HMGCS1 and SQLE were differentially expressed supporting increased membrane production. Indeed, histological analysis of COVID-19 patient biopsies reveals enlarged lung epithelial cells with amphophilic granular cytoplasm due to the abundance of replication membranes (Xu et al., 2020). Transmission electron microscopy images of SARS-CoV-2 infected lung cells show the presence of lipid droplets in close association to the virus replication membranes (Pizzorno et al., 2020). It is important to note that lipogenesis is poorly tolerated in thin epithelial tissue potentially leading to pulmonary lipotoxicity (Plantier et al., 2012).

Transcriptional regulatory analysis showed the induction of lipogenesis by C/EBP and PPARγ, as well as the suppression of fatty acid oxidation by PPARα inhibition. PPARα downregulated target genes like CPT1A block mitochondrial fatty acid oxidation (**Fig. 3A**). These results support some of the recent observations of lipid accumulation in SARS, MERS, and influenza virus infection of different cell lines (Episcopio et al., 2019; Yan et al., 2019a). However, in contrast to these earlier studies, SARS-CoV-2 infection of primary cells did not appear to involve SREBP. Interestingly, HCV infection of primary hepatocytes induced fatty acid oxidation and suppressed cholesterol synthesis (Levy et al., 2016) the exact opposite of SARS-CoV-2 infection of primary lung cells (**Fig. 2C**).

These results suggest that PPARα activation of fatty acid oxidation using fenofibrate (Tricor®) could disrupt the SARS-CoV-2 lifecycle, while PPARγ activation using rosiglitazone (Avandia®) would not. Indeed, treatment of SARS-CoV-2 infected cells with fenofibrate blocked phospholipid accumulation and increased glycolysis, reversing the metabolic effects of infection (**Fig. 4C-E**). Viral replication was effectively blocked, reduced by 3-log over 5 days period to below our assay detection limit, while cell viability was unaffected (**Fig. 4F; Supplement Fig. S3**). These results stand in contrast to rosiglitazone which didn't affect the metabolic pathway or viral load, possibly due to the already active state of PPARγ. Inhibition of PPARγ by GW9662 showed a marginal effect, correcting lipid metabolism, but not significantly affecting glycolysis or viral replication. Interestingly, antitussive cloperastine (Hustazol®) recently identified as an SGLT1 inhibitor, significantly reduced viral load by 3-fold without affecting cell viability. (**Fig. 4F; Supplement Fig. S3**).

This work charts the transcriptional fingerprint induced by SARS-CoV-2 infection on lung metabolism. The virus shows a distinct metabolic signature dominated on one hand by transcriptional induction of a *Warburg effect* through NFκB and RELA, and on the other hand by ER stress-induced lipid accumulation mediated by C/EBP, PPARγ, and PPARα. These pathways are interwoven and support efficient viral replication, assembly, and egress. Disruption of lipid metabolism through PPARα activation could prove an effective therapeutic target in the ongoing battle against COVID-19.

Acknowledgments

Funding was provided by European Research Council Consolidator Grants OCLD (project no. 681870) and generous gifts from the Nikoh Foundation and the Sam and Rina Frankel Foundation (YN). This work was additionally funded by generous support from the Marc Haas Foundation, the National Institutes of Health, and DARPA's PREPARE Program (HR0011-20-2-0040). The views, opinions, and/or findings expressed are those of the author and should not be interpreted as representing the official views or policies of the Department of Defense or the U.S. government (BRT).

STAR METHODS

KEY RESOURCES TABLE

REAGENT or RESOURCE	SOURCE	IDENTIFIER
Antibodies		
Bacterial and Virus Strains		
SARS-related coronavirus 2 (SARS-CoV-2), Isolate USA-WA1/2020	CDC; BEI Resources, NIAID, NIH	NR-52281
Ampicillin resistant NEB Stable Bacteria with pLVX-EF1alpha-IRES-Puro backbone inserted with Plasmids encoding the SARS-CoV-2 open reading frames (ORFs) and eGFP	Addgene; Nevan Krogan	#141367-141395
Biological Samples		
COVID19-infected human lung biopsy	Weill Cornell Medicine.	
Uninfected human lung biopsy	Mount Sinai Institutional Biorepository and Molecular Pathology Shared Resource Facility (SRF) in the Department of Pathology.	
Chemicals, Peptides, and Recombinant Proteins		

Bronchial epithelial growth media; SingleQuots	Lonza	CC-3171; CC-4175
Airway epithelial cell basal media; Bronchial Epithelial Growth Kit	ATCC	PCS-300-030; PCS-300-040
Cloperastine	Merck	C2040
Empagliflozin	AdipoGen	AG-CR1-3619
Metformin	Merck	317240
Fenofibrate	Merck	F6020
Rosiglitazone	Merck	R2408
GW9662	Merck	M6191
2-(N-(7-Nitrobenz-2-oxa-1,3-diazol-4-yl) Amino)-2-Deoxyglucose (2-NDBG)	Invitrogen	N13195
JC-1 dye	Invitrogen	T3168
Critical Commercial Assays		
HCS LipidTOX™ Phospholipidosis and Steatosis Detection Kit	ThermoFisher	H34158
Accutrend Plus multiparameter meter; Accutrend Plus Glucose and BM-Lactate Test Strips	Roche Diagnostics	
Mitochondrial Stress Test Kit	Agilent	103015-100
Deposited Data		
Transcriptome of mock and infected NHBEC, healthy and infected lung biopsy	RNA-Seq	GSE135713
Experimental Models: Cell Lines		
Normal human bronchial epithelial cells (NHBEC; 79-year-old Caucasian female)	Lonza	CC-2540 Lot# 580580
Normal human bronchial epithelial cells (NHBEC; 14-year-old Hispanic male)	ATCC	PCS-300-010 Lot#70002486
Software and Algorithms		
RSEM	(Li and Dewey, 2011)	https://github.com/deweylab/RSEM
DESeq2	(Love et al., 2014)	https://bioconductor.org/packages/release/bioc/html/DESeq2.html
Bowtie2	(Langmead and Salzberg, 2012)	http://bowtie-bio.sourceforge.net/bowtie2/index.shtml
prcomp package	(Sigg and Buhmann, 2008)	https://stat.ethz.ch/R-manual/R-devel/library/stats/html/prcomp.html
ggplot2	(Wickham, 2009)	https://github.com/tidyverse/ggplot2
Morpheus	Broad Institute	https://software.broadinstitute.org/morpheus

DAVID Informatics Resources 6.7	(Huang da et al., 2009)	david.ncifcrf.gov
fastp v20	(Chen, Zhou et al. 2018)	https://github.com/OpenGene/fastp.git
Kallisto version 0.46.1		https://github.com/pachterlab/kallisto
PANTHER Classification System	(Mi, Muruganujan et al. 2018)	http://geneontology.org/
GeneMania	(Mostafavi, Ray et al. 2008)	https://genemania.org/
McGill's Network Analyst Tool	(Xia et al., 2015)	https://www.networkanalyst.ca/
ImageJ2	(Rueden et al., 2017)	https://imagej.net/ImageJ2
Fiji	(Schindelin et al., 2012)	https://fiji.sc/
CellProfiler	(Carpenter et al., 2006)	https://cellprofiler.org/
CellProfiler Single Cell Pipeline		https://github.com/avnere/Single-Cell-Analysis-CellProfiler-Pipeline.
MsigDB v7.1	(Liberzon, Birger et al. 2015)	
Trrust TF database v2	(Han, Cho et al. 2018)	
RegNetwork	(Liu, Wu et al. 2015)	
RStudio Desktop	RStudio	https://rstudio.com/
R version 4.0.2/3.6.3		https://www.r-project.org/
Basespace	Illumina	

CONTACT FOR REAGENT AND RESOURCE SHARING

Further information and requests for reagents may be directed to and will be fulfilled by the corresponding author Yaakov Nahmias (ynahmias@cs.huji.ac.il).

EXPERIMENTAL MODEL AND SUBJECT DETAILS

Human Subjects

All protocols involving human tissue were reviewed and exempted by the Hebrew University of Jerusalem and Weill Cornell Medical College Institutional Review Boards.

Cell Culture

Normal human bronchial epithelial (NHBE) cells (Lonza, CC-2540 Lot# 580580), isolated from a 79-year-old Caucasian female and were maintained at 37°C and 5% CO_2 in bronchial epithelial growth media (Lonza, CC-3171) supplemented with SingleQuots (Lonza, CC-4175) per manufacturer's instructions. Cells were maintained at the BSL3 facilities of the Icahn School of Medicine at Mount Sinai. NHBE cells (ATCC, PCS-300-010 Lot#70002486), isolated from a 14-year-old Hispanic male were maintained in airway epithelial cell basal media (ATCC, PCS-300-030) supplemented with Bronchial Epithelial Growth Kit as per the manufacturer's instructions (ATCC, PCS-300-040) at 37°C and 5% CO_2. Cells were maintained at the BSL2 facilities of the Hebrew University of Jerusalem.

Viruses
SARS-related coronavirus 2 (SARS-CoV-2), Isolate USA-WA1/2020 (NR-52281) was deposited by the Center for Disease Control and Prevention and obtained through BEI Resources, NIAID, NIH. SARS-CoV-2 was propagated in Vero E6 cells in DMEM supplemented with 2% Fetal Bovine Serum (FBS), 4.5 g/L D-glucose, 4 mM L-glutamine, 10 mM Non-Essential Amino Acids (NEAA), 1 mM Sodium Pyruvate and 10 mM HEPES. Infectious titers of SARS-CoV-2 were determined by plaque assay in Vero E6 cells in Minimum Essential Media (MEM) supplemented with 4 mM L-glutamine, 0.2% Bovine Serum Albumin (BSA), 10 mM HEPES and 0.12% $NaHCO_3$ and 0.7% agar.

All work involving live SARS-CoV-2 was performed in the CDC/USDA-approved BSL-3 facility of the Global Health and Emerging Pathogens Institute at the Icahn School of Medicine at Mount Sinai in accordance with institutional biosafety requirements.

COVID-19 Biopsy Samples
For RNA analysis, two COVID19 human subjects were deceased upon tissue acquisition and were provided from Weill Cornell Medicine as fixed samples. Uninfected human lung samples (n=2) were obtained post-surgery through the Mount Sinai Institutional Biorepository and Molecular Pathology Shared Resource Facility (SRF) in the Department of Pathology. The Biorepository operates under a Mount Sinai Institutional Review Board (IRB) approved protocol and follows guidelines set by HIPAA.

METHOD DETAILS

Drug Treatments
Approximately 5×10^5 NHBE cells were infected with SARS-CoV-2 at a MOI of 2 in bronchial epithelial growth media. Culture media was supplemented with 0.1% DMSO (vehicle control), 10 μM Cloperastine (Merck; C2040), 5 μM Empagliflozin (AG-CR1-3619), 1 mM Metformin (Merck; 317240), 20 μM Fenofibrate (Merck; F6020) , 20 μM Rosiglitazone (Merck; R2408) or 10 μM GW9662 (Merck; M6191). After 24h, the media was collected and changed to bronchial epithelial growth media with the respective drug at the concentration listed above. Then, every 48 hours media was collected and replenished. The media was stored in -80ºC immediately after removal.

Bioinformatic Analyses
Raw reads were aligned to the human genome (hg19) using the RNA-Seq Alignment App on Basespace (Illumina, CA), following differential expression analysis using DESeq2 (Love et al., 2014). Differentially expressed genes (DEGs) were characterized for each sample (p adjusted-value < 0.05) and were used as a query to search for enriched biological processes (Gene ontology BP) and network analysis of protein interactions using STRING14. Heatmaps of gene expression levels were constructing using heatmap from the ggplot package in (Liu, Wu et al. 2015 (https://cran.r- project.org/web/packages/gplots/index.html).

Analysis of Canonical Splice Variants
Reads were downloaded from SRA (GSE147507), and filtered and trimmed to remove low-quality reads and sequencing artifacts with fastp v20 (Chen et al., 2018) (https://github.com/OpenGene/fastp.git). Reads were pseudoaligned to the GRCh38 genecode human transcriptome (GRCh38.p13, version 32) using Kallisto version 0.46.1 (https://github.com/pachterlab/kallisto) run with the default k-mer length of 31, in single-read, single-overhang mode, with fragment mean length of 400 and 100 SD. Differentially expressed

transcripts/genes were identified using Sleuth based on a likelihood ratio test comparing the condition of interest and 100 Kallisto bootstrap samples.

Quantification of Intracellular Glucose

To detect glucose uptake, we used 2-(N-(7-Nitrobenz-2-oxa-1,3-diazol-4-yl) Amino)-2-Deoxyglucose (2-NDBG) a fluorescent analog of glucose (Invitrogen, USA; N13195). 2-NDBG is transported through SGLT-1 and GLUT-2. Increased uptake leads to 2-NDBG accumulation in the cells. Cells infected with SARS-CoV-2 for 96 hours were exposed to 6 mM of 2-NDBG for 24 hours. Cells were then fixed, counterstained with 1 µg/mL Hoechst 33258. Staining intensity was normalized to Hoechst 33258 across multiple fields of view.

Quantification of Lipid

Lipid accumulation was measured using HCS LipidTOX™ Phospholipidosis and Steatosis Detection Kit according to the manufacturer's instructions (ThermoFisher, USA; H34158). Briefly, cells were incubated in complete bronchial epithelial growth media supplemented with 1x phospholipidosis detection reagent for 48 hours. Cells were subsequently fixed in 4% PFA and stained with 1X neutral lipid detected reagent for 30 min and counterstained with 1 µg mL-1 Hoechst 33258. Staining intensity was normalized to the amount of Hoechst 33258 positive nuclei across multiple fields of view.

Mitochondrial Membrane Potential

Mitochondrial membrane potential ($\Delta\psi_m$), was estimated using JC-1 dye according to the manufacturer's instructions (Invitrogen, USA; T3168). Cells were incubated with 5µM JC-1 dye in complete bronchial epithelial growth media supplemented for 30 min, washed with PBS, and incubated with complete bronchial epithelial growth media supplemented. Wells were excited at 488 nm and 570 nm and the ratio between green (530 nm) and red (590 nm) mean intensity value emissions light was calculated for each measurement. The intensity was normalized to the amount of Hoechst 33258 positive nuclei.

Metabolic of Analysis Glucose, Lactate, and Glutamine

For metabolic analysis of SARS-CoV-2 infected culture media in the BSL3 facility, we used the Accutrend Plus multiparameter meter (Roche Diagnostics). Culture media was collected every 48 hours and stored at -80 ºC prior to analysis. Measurements were carried out using Accutrend Plus Glucose and BM-Lactate Test Strips according to the manufacturer's instructions. Metabolic analysis of cells cultured in BSL2 facility used the more complete amperometric glucose, lactate, and glutamine sensor array (IST, Switzerland) as previously described (Ehrlich et al., 2018). Measurements were carried out on 3 biological repeats using 2 technical repeats, calibrated throughout the measurement using a calibration media. In both measurements, glucose and glutamine uptake as well as lactate production were calculated based on the difference between sample and control media.

Generation Lentiviral SARS-CoV-2 constructs

Plasmids encoding the SARS-CoV-2 open reading frames (ORFs) and eGFP control are a kind gift of Nevan Krogan (Addgene plasmid #141367-141395). Plasmids were acquired as bacterial LB-agar stabs, and used per the provider's instructions. Briefly, each stab was first seeded into agar LB (Bacto Agar; BD, USA) in 10 cm plates. Then, single colonies are inculcated into flasks containing LB (BD Difco LB Broth, Lennox; BD, USA) and 100 µg/ml penicillin (BI, Israel). Transfection grade plasmid DNA was isolated from each flask using the ZymoPURE II Plasmid Maxiprep Kit (Zymo Research, USA) according to the manufacturer's instructions.

HEK 293T cells (ATCC, USA) were seeded in 10 cm cell culture plates at a density of $4x10^6$ cells/plate. The cells were maintained in 293T medium composed of DMEM high glucose (4.5 g/l; Merck, USA) supplemented with 10% FBS (BI, Israel), 1x NEAA (BI, Israel), and 2 mM L-alanine-L-glutamine (BI, Israel).

The following day, the cells were transfected with a SARS CoV 2 orf-expressing plasmid and the packaging plasmids using the TransIT-LT1 transfection reagent (Mirus Bio, USA) according to provider's instructions. Briefly, 6.65ug SARS CoV 2 lentivector plasmid, 3.3µg pVSV-G, and 5µg psPAX2 were mixed in Opti-MEM reduced serum medium (Gibco, USA), with 45ul of TransIT-LT1, and kept in room temperature to complex and then added to each plate. Following 18h of incubation, the transfection medium was replaced with 293T medium and virus-rich supernatant was harvested after 48h and 96h. The supernatant was clarified by centrifugation (500xg, 5min) and filtration (0.45um, Millex-HV, MerckMillipore). All virus stocks were aliquoted and stored at -80oC.

The packaging plasmids (psPAX2 and pVSV-G) are a kind gift from Prof. N. Benvenisti, Stem Cell Unit at the Hebrew University, Jerusalem, Israel.

SARS-CoV-2 proteins lentiviral transduction

Approximately 1×10^5 cells were infected in two consecutive sessions of 12h each. A 50% dilution of the viral stock was used both for a final transduction efficiency of ~60%. transduction efficiency was validated by microscopy of the eGFP transduced culture.

RNA-Seq of Viral Infections

Approximately 1×10^5 NHBE cells were infected with SARS-CoV-2 at a MOI of 2 for 24 h in bronchial epithelial growth media supplemented with BEGM SingleQuots. Total RNA from infected and mock-infected cells was extracted using TRIzol Reagent (Invitrogen) and Direct-zol RNA Miniprep kit (Zymo Research) according to the manufacturer's instructions and treated with DNase I. RNA-seq libraries of polyadenylated RNA were prepared using the TruSeq RNA Library Prep Kit v2 (Illumina) according to the manufacturer's instructions. RNA-seq libraries for total ribosomal RNA-depleted RNA were prepared using the TruSeq Stranded Total RNA Library Prep Gold (Illumina) according to the manufacturer's instructions. cDNA libraries were sequenced using an Illumina NextSeq 500 platform**.**

Viral Load Quantitative Real-Time PCR Analysis

Genomic viral RNA was extracted from supernatants using TRIzol reagent according to the manufacturer's instructions (Thermo Fisher). RNA was reverse transcribed into cDNA using oligo d(T) primers and SuperScript II Reverse Transcriptase (Thermo Fisher). Quantitative real-time PCR was performed on a LightCycler 480 Instrument II (Roche) using KAPA SYBR FAST qPCR Master Mix Kit (KAPA biosystems and primers specific for the SARS-CoV-2 nsp14 transcript as described previously (Chu et al., 2020, Corman et al., 2020). The viral load for each sample was determined using genomic viral RNA purified from viral stocks to generate a standard curve. Error bars indicate the standard error from three biological replicates.

Processing, Analysis, and Graphic Display of Genomic Data

Hierarchical clustering, heat maps, correlation plots, and similarity matrices were created in Morpheus. Gene ontology enrichment analyses and clustering were performed using DAVID Informatics Resources 6.7 [49] and PANTHER Classification System (Mi et al., 2018). Metabolic

network maps were created using McGill's Network Analyst Tool using the KEGG database [50]. Transcription factor networks were created using GeneMania (Mostafavi et al., 2008).

Assembly of Metabolic Categories

Aggregate metabolic categories were created as previously described (Levy et al., 2016). Briefly, functional annotation gene-sets, taken from GO and KEGG, were merged into a set of glucose, lipid, mitochondrial, and amino acid gene-sets (Supplementary Table 1).

Metabolic Flux Quantification (SeaHorse)

Mitochondrial Stress Test assay was conducted per manufacturer instructions as previously described(Levy et al., 2016). Briefly, cells were incubated in unbuffered DMEM supplemented with 2 mM glutamine, 1 mM sodium pyruvate, and 10 mM glucose (pH 7.4) for 1 hour at 37°C in a non-CO_2 incubator. Basal oxygen consumption rate (OCR) was measured for 30 min, followed by injection of 1.5 μM oligomycin, a mitochondrial Complex V inhibitor that blocks oxidative phosphorylation. The decrease in OCR due to oligomycin treatment is defined as oxidative phosphorylation rate. 0.5 μM carbonyl cyanide-4 (trifluoromethoxy) phenylhydrazone (FCCP), an uncoupling agent, is added at 60 min to measure maximal mitochondrial activity followed by complete inhibition at 90 min using a mixture of 0.5 μM antimycin A and rotenone, mitochondrial Complex III and Complex I inhibitors.

Functional Annotations of Gene Expression

Differentially expressed genes were tested for enrichment overlap within functional gene sets. The general test for functional enrichment of the differentially expressed genes against various functional categories was done using the PANTHER tool (Mi et al., 2018). We tested the enrichment of differentially expressed genes with metabolic categories (defined above), using the intersection of in-vitro expressed genes and all genes with GO annotation as the background list (N=20851). Enrichment P values were calculated using Fisher's exact test and corrected with family-wise (Bonferroni) multiple hypotheses correction or Benjamini & Hochberg False discovery procedure as indicated.

Transcription Factor Target Genes

Transcription factor (TF) gene targets were aggregated from the following databases: MsigDB v7.1 (Liberzon et al., 2015), Trrust TF database v2 (Han et al., 2018), RegNetwork (Liu et al., 2015). Enrichment of TF targets among differentially expressed genes, stratified by selected metabolic gene categories (see above) was tested with a hypergeometric enrichment test, and adjusted for false discovery rate using a Benjamini & Hochberg procedure.

Ethical Statement

Experiments using samples from human subjects were conducted in accordance with local regulations and with the approval of the institutional review board at the Icahn School of Medicine at Mount Sinai under protocol HS#12-00145.

Quantification and Statistical Analysis

All experiments were done in at least 3 biological repeats. Measurements were done in either technical triplicates or quadruplets, images were analyzed with 5 or more fields of view; Graphs show mean ± SEM; Continuous variables were calculated using Mann-Whitney Rank Sum or Student's t-test, categorical variables with chi-square, and ANOVA tests.

Pairwise comparisons were performed using Student's t-test; Mann-Whitney U test was used when the distribution could not be determined to be normal; FDR correction was used to adjust

for multiple comparisons and RNA seq comparisons; Hypergeometric testing was used to assess statistically significant enrichments. * indicates $p < 0.05$, ** indicates $p < 0.01$, *** indicates $p < 0.001$, unless denoted otherwise**.**

Data and Software Availability

Data resources
Data that support the findings displayed in this study have been deposited in Mendeley Data. Sequencing data that support the findings in this study have been deposited in GEO with the accession code GSE135713.

Software resources
Our custom Cell Analysis CellProfiler® Pipeline is available on https://github.com/avnere/Single-Cell-Analysis-CellProfiler-Pipeline.

Figure Legends

Figure 1. Transcriptional metabolic signature of SARS-CoV-2 infection. (**A**) Dot plot visualization of enriched GO terms in SARS-CoV-2 infected lung biopsies (n=2, $p<0.05$) and primary bronchial epithelium culture (n=3, $p<0.05$). Enrichment analysis shows the viral induction of immune response and inflammation as well as cellular stress (FDR$<10^{-22}$) and lipid metabolism (FDR$<10^{-5}$). (**B**) Venn diagram describing the relationship between differentially expressed genes (DEG), metabolic genes (GO:0008152), and lipid metabolism genes (GO:0006629) in of SARS-CoV-2 infection in primary lung cells and COVID-19 patient biopsies. The analysis shows that the majority of the transcriptional response is associated with metabolic processes. (**C**) Sunburst graph showing the coverage of our composite metabolic terms on general metabolic response induced by SARS-CoV-2 infection of primary lung cells and COVID-19 patient biopsies. Lipid and mitochondrial metabolism dominate the transcriptional metabolic signature of infection. (**D**) Schematic depicting the metabolic landscape of SARS-CoV-2 infection superimposed with a heat map of pathway-associated metabolic and stress genes. Red and green boxes are up and downregulated by infection, respectively. * marks differentially regulated genes (n=3, FDR<0.05). Black arrows represent metabolic pathways differentially regulated by the transcriptional response to SARS-CoV-2 infection (n=3, FDR <0.01). Blue arrows represent the orchestrated induction of endoplasmic and mitochondrial stress.

Figure 2. SARS-CoV-2 induces endoplasmic stress and lipid accumulation. (**A**) Schematic depicting ER stress pathways superimposed with pathway-associated genes. Red and green boxes are up and downregulated by infection, respectively. * marks differentially regulated genes (n=3, FDR<0.05). Red and green arrows schematically note interactions based on the transcriptional response. XBP1S is the IRE1 spliced form of XBP1. (**B**) Schematics of the pathway-specific interactions between viral proteins (black), host protein (green), and the main genes in each ER stress pathway (blue). JNK and PP1 appear to physically interact with numerous viral proteins. (**C**) Schematic of lipid metabolism fluxes. Genes changed by SARS-CoV-2 infection are marked red and green for up and downregulation, respectively. * marks differentially regulated genes (n=3, FDR <0.01). (**D**) Fluorescence images of primary bronchial epithelial cells infected with SARS-CoV-2 virus or mock control. Neutral lipids (triglycerides) are dyed green while phospholipids are dyed red (*methods*). Image analysis shows a 20% increase in intracellular lipids following SARS-CoV-2 infection. (n=3; Bar = 10 µm). (**E**) Transcriptional regulatory analysis highlights transcription factors whose target genes are

differentially regulated in lipid metabolism. A large cluster of interconnected transcription factors appears to play a role in lipid metabolism including NFκB, RELA, and SP1 as well as the lipid-activated nuclear receptors PPARα and PPARγ. Heat map of regulators of lipid metabolism identified in COVID-19 patient biopsies and SARS-CoV-2 infected lung cells. The activity of NFκB, RELA, SP1, and PPARα was validated in patient samples. (**F**) Schematic of the interactions between viral proteins (black), host protein (greens), with key genes and transcription factors controlling the metabolic pathway. Viral NSP7 interacts with PPARα, PPARγ, and RXRα through ACSL3 and with SREBP and CEBPB through SCARB1. BCKDK which drives HMG-CoA production is directly bound by viral NSP12. Viral NSP7 interacts with both ACAT1 and ACAA1 through RHOA. (**G**) Microscopic analysis of lipid accumulation in primary epithelial cells expressing individual viral proteins compared to mock control. Cells expressing viral protein M, NSP5, and NSP7 showed a 50% increase in neutral and phospholipids (n=3; Bar = 20 μm).

Figure 3. SARS-CoV-2 induces a *Warburg*-like effect in primary cells. (**A**) Schematic of citric acid cycle fluxes. Genes changed by SARS-CoV-2 infection are marked red and green for up and downregulation, respectively. * marks differentially regulated genes (n=3, FDR <0.01). (**B**) Transcriptional regulatory analysis highlights transcription factors whose target genes are differentially regulated in mitochondrial metabolism including NFκB, RELA, SP1, and JUN. Heat map of regulators of mitochondrial metabolism identified in COVID-19 biopsies confirms that activation of NFκB, RELA, SP1, and JUN targets in patients. (**C**) Schematic of the interactions between viral proteins (black), host protein (green), transcription factors, and enzymes controlling the metabolic pathway. Viral NSP7 has had multiple physical interactions with enzymes of the citric acid cycle through QSOX2, RAB, ACSL3, and RHOA. Viral ORF3a and NSP5 interact with RELA and NFκB through HMOX1 and HDAC2. (**D**) Microscopic analysis of mitochondrial membrane potential (ΔΨm) in primary epithelial cells expressing individual viral proteins compared to mock control. Expression of NSP7 caused a significant 65% decrease in the mitochondrial membrane potential ($p<0.01$), while the expression of ORF6 and ORF3a had a milder effect. (n=3; Bar = 50 μm). (**E**) Schematic of glucose metabolism fluxes. Genes changed by SARS-CoV-2 infection are marked red and green for up and downregulation, respectively. * marks differentially regulated genes (n=3, FDR <0.01). (**F**) Transcriptional regulatory analysis highlights transcription factors whose target genes are differentially regulated in glucose metabolism. NFκB, RELA, and GATA6 form a distinct cluster in the transcription factor network. Heat map of regulators of glucose metabolism identified in COVID-19 patient biopsies and SARS-CoV-2 infected lung cells confirms NFκB and RELA activation in patient samples. (**G**) Metabolic analysis of SARS-CoV-2 and mock-infected primary lung cells shows a 50% increase ($p<0.001$) in lactate production. (**H**) Fluorescence images of primary bronchial epithelial cells infected with SARS-CoV-2 virus or mock control. Cells show intracellular accumulation of 2-NDBG a fluorescent glucose analog (n=3; Bar = 40 μm). (**I**) Schematic of the interactions between viral proteins (black), host protein (green), transcription factors, and enzyme (orange) of glucose metabolism. Viral ORF3a interacts with both RELA and NFκB through HMOX1. Viral NSP7 interacts with both TPI1 and PKM through CYB5R3. (**J**) Metabolic analysis of primary epithelial cells expressing individual viral proteins compared to mock control. Expression of NSP7, NSP5, and ORF3a caused a significant 14% increase in the lactate of glucose ratio, indicating a shift to glycolysis.

Figure 4. Emerging therapeutic targets of SARS-CoV-2 induced host metabolic pathways. (**A**) Schematic depicting the metabolic landscape of SARS-CoV-2 infection superimposed with transcription factors found to regulate each pathway. Potential drug (white boxes) and their therapeutic targets are marked on the chart. (**B**) Table summarizing potential drugs, dietary supplements, and experimental molecules that can potentially reverse SARS-CoV-2 induced metabolic alterations. (**C**) Microscopic analysis of lipid accumulation in SARS-CoV-2 infected lung cells exposed to different drugs for 5 days compared to DMSO-treated (vehicle) and mock-infected controls. Cells treated with PPARα agonist fenofibrate had lower phospholipid content, with neutral lipids packed in lipid droplets. Cells treated GW9662 showed decreased phospholipid and neutral lipid accumulation, but also noted a loss of cell viability. (**D**) Image-based quantification of neutral lipid and phospholipids. (**E**) Lactate over glucose ratio of SARS-CoV-2 infected primary lung cells treated with various drugs. Fenofibrate significantly reduced the lactate to glucose ratio by 60% ($p<0.01$) normalizing the metabolic shift induced by infection (n=3; Bar = 50 µm). (**F**) Quantification of SARS-CoV-2 virion particles over 5 days of treatment with various drugs or DMSO (vehicle). Treatment with 20 µM fenofibrate reduced SARS-CoV-2 viral load by 2-logs close to the detection limit of the assay (n=3; $p<0.001$). Treatment with 10 µM GW992 or 10 µM cloperastine reduced viral load by 2.5 to 3-fold (n=3; $p<0.05$).

References

Blanco-Melo, D., Nilsson-Payant, B.E., Liu, W.-C., Uhl, S., Hoagland, D., Møller, R., Jordan, T.X., Oishi, K., Panis, M., Sachs, D., *et al.* (2020). Imbalanced Host Response to SARS-CoV-2 Drives Development of COVID-19. Cell *181*, 1036-1045.e1039.

Bornstein, S.R., Dalan, R., Hopkins, D., Mingrone, G., and Boehm, B.O. (2020). Endocrine and metabolic link to coronavirus infection. Nature Reviews Endocrinology.

Burggraaff, L., Oranje, P., Gouka, R., van der Pijl, P., Geldof, M., van Vlijmen, H.W.T., Ijzerman, A.P., and van Westen, G.J.P. (2019). Identification of novel small molecule inhibitors for solute carrier SGLT1 using proteochemometric modeling. Journal of Cheminformatics *11*, 15.

Chen, S., Zhou, Y., Chen, Y., and Gu, J. (2018). fastp: an ultra-fast all-in-one FASTQ preprocessor. Bioinformatics *34*, i884-i890.

Ehrlich, A., Tsytkin-Kirschenzweig, S., Ioannidis, K., Ayyash, M., Riu, A., Note, R., Ouedraogo, G., Vanfleteren, J., Cohen, M., and Nahmias, Y. (2018). Microphysiological flux balance platform unravels the dynamics of drug induced steatosis. Lab on a Chip *18*, 2510-2522.

Episcopio, D., Aminov, S., Benjamin, S., Germain, G., Datan, E., Landazuri, J., Lockshin, R.A., and Zakeri, Z. (2019). Atorvastatin restricts the ability of influenza virus to generate lipid droplets and severely suppresses the replication of the virus. The FASEB Journal *33*, 9516-9525.

Fujita, N., Kaito, M., Kai, M., Sugimoto, R., Tanaka, H., Horiike, S., Konishi, M., Iwasa, M., Watanabe, S., and Adachi, Y. (2006). Effects of bezafibrate in patients with chronic hepatitis C virus infection: combination with interferon and ribavirin. J Viral Hepat *13*, 441-448.

Fung, T.S., and Liu, D.X. (2019). Human Coronavirus: Host-Pathogen Interaction. Annu Rev Microbiol *73*, 529-557.

Gordon, D.E., Jang, G.M., Bouhaddou, M., Xu, J., Obernier, K., O'Meara, M.J., Guo, J.Z., Swaney, D.L., Tummino, T.A., Huettenhain, R., *et al.* (2020). A SARS-CoV-2-Human Protein-Protein Interaction Map Reveals Drug Targets and Potential Drug-Repurposing. bioRxiv, 2020.2003.2022.002386.

Gualdoni, G.A., Mayer, K.A., Kapsch, A.M., Kreuzberg, K., Puck, A., Kienzl, P., Oberndorfer, F., Fruhwirth, K., Winkler, S., Blaas, D., *et al.* (2018). Rhinovirus induces an anabolic reprogramming in host cell metabolism essential for viral replication. Proc Natl Acad Sci U S A *115*, E7158-e7165.

Han, H., Cho, J.W., Lee, S., Yun, A., Kim, H., Bae, D., Yang, S., Kim, C.Y., Lee, M., Kim, E., *et al.* (2018). TRRUST v2: an expanded reference database of human and mouse transcriptional regulatory interactions. Nucleic Acids Res *46*, D380-D386.

Han, J., and Kaufman, R.J. (2016). The role of ER stress in lipid metabolism and lipotoxicity. J Lipid Res *57*, 1329-1338.

Hassan, I.H., Zhang, M.S., Powers, L.S., Shao, J.Q., Baltrusaitis, J., Rutkowski, D.T., Legge, K., and Monick, M.M. (2012). Influenza A viral replication is blocked by inhibition of the inositol-requiring enzyme 1 (IRE1) stress pathway. The Journal of biological chemistry *287*, 4679-4689.

Ikeda, M., Abe, K., Yamada, M., Dansako, H., Naka, K., and Kato, N. (2006). Different anti-HCV profiles of statins and their potential for combination therapy with interferon. Hepatology *44*, 117-125.

Kilbourne, E.D. (1959). Inhibition of influenza virus multiplication with a glucose antimetabolite (2-deoxy-D-glucose). Nature *183*, 271-272.

Latif Reshi, H.-V.W.a.J.-R.H. (2018). Modulation of Mitochondria During Viral Infections. In Mitochondrial Diseases, E.T.a.C.G.a.Y. Sevgiler, ed. (IntechOpen).

Levy, G., Habib, N., Guzzardi, M.A., Kitsberg, D., Bomze, D., Ezra, E., Uygun, B.E., Uygun, K., Trippler, M., Schlaak, J.F., *et al.* (2016). Nuclear receptors control pro-viral and antiviral metabolic responses to hepatitis C virus infection. Nature Chemical Biology *12*, 1037-1045.

Liberzon, A., Birger, C., Thorvaldsdottir, H., Ghandi, M., Mesirov, J.P., and Tamayo, P. (2015). The Molecular Signatures Database (MSigDB) hallmark gene set collection. Cell Syst *1*, 417-425.

Liu, Z.P., Wu, C., Miao, H., and Wu, H. (2015). RegNetwork: an integrated database of transcriptional and post-transcriptional regulatory networks in human and mouse. Database (Oxford) *2015*.

Love, M.I., Huber, W., and Anders, S. (2014). Moderated estimation of fold change and dispersion for RNA-seq data with DESeq2. Genome Biology *15*, 550.

Mayer, K.A., Stöckl, J., Zlabinger, G.J., and Gualdoni, G.A. (2019). Hijacking the Supplies: Metabolism as a Novel Facet of Virus-Host Interaction. Frontiers in Immunology *10*.

McBride, C.E., and Machamer, C.E. (2010). Palmitoylation of SARS-CoV S protein is necessary for partitioning into detergent-resistant membranes and cell-cell fusion but not interaction with M protein. Virology *405*, 139-148.

Mi, H., Muruganujan, A., Ebert, D., Huang, X., and Thomas, P.D. (2018). PANTHER version 14: more genomes, a new PANTHER GO-slim and improvements in enrichment analysis tools. Nucleic Acids Research *47*, D419-D426.

Mostafavi, S., Ray, D., Warde-Farley, D., Grouios, C., and Morris, Q. (2008). GeneMANIA: a real-time multiple association network integration algorithm for predicting gene function. Genome Biol *9 Suppl 1*, S4.

Oranje, P., Gouka, R., Burggraaff, L., Vermeer, M., Chalet, C., Duchateau, G., van der Pijl, P., Geldof, M., de Roo, N., Clauwaert, F., *et al.* (2019). Novel natural and synthetic inhibitors of solute carriers SGLT1 and SGLT2. Pharmacol Res Perspect *7*, e00504-e00504.

Pizzorno, A., Padey, B., Julien, T., Trouillet-Assant, S., Traversier, A., Errazuriz-Cerda, E., Fouret, J., Dubois, J., Gaymard, A., Lescure, F.-X., *et al.* (2020). Characterization and treatment of SARS-CoV-2 in nasal and bronchial human airway epithelia. bioRxiv, 2020.2003.2031.017889.

Plantier, L., Besnard, V., Xu, Y., Ikegami, M., Wert, S.E., Hunt, A.N., Postle, A.D., and Whitsett, J.A. (2012). Activation of sterol-response element-binding proteins (SREBP) in alveolar type II cells enhances lipogenesis causing pulmonary lipotoxicity. J Biol Chem *287*, 10099-10114.

Shi, C.-S., Nabar, N.R., Huang, N.-N., and Kehrl, J.H. (2019). SARS-Coronavirus Open Reading Frame-8b triggers intracellular stress pathways and activates NLRP3 inflammasomes. Cell Death Discovery *5*, 101.

Smallwood, H.S., Duan, S., Morfouace, M., Rezinciuc, S., Shulkin, B.L., Shelat, A., Zink, E.E., Milasta, S., Bajracharya, R., Oluwaseum, A.J., *et al.* (2017). Targeting Metabolic Reprogramming by Influenza Infection for Therapeutic Intervention. Cell Rep *19*, 1640-1653.

Son, Y.O., Heo, J.S., Kim, T.G., Jeon, Y.M., Kim, J.G., and Lee, J.C. (2010). Over-expression of JunB inhibits mitochondrial stress and cytotoxicity in human lymphoma cells exposed to chronic oxidative stress. BMB Rep *43*, 57-61.

Takahashi, T., and Suzuki, T. (2011). Function of membrane rafts in viral lifecycles and host cellular response. Biochem Res Int *2011*, 245090-245090.

Wu, Q., Zhou, L., Sun, X., Yan, Z., Hu, C., Wu, J., Xu, L., Li, X., Liu, H., Yin, P., *et al.* (2017). Altered Lipid Metabolism in Recovered SARS Patients Twelve Years after Infection. Scientific Reports *7*, 9110.

Xu, Z., Shi, L., Wang, Y., Zhang, J., Huang, L., Zhang, C., Liu, S., Zhao, P., Liu, H., Zhu, L., *et al.* (2020). Pathological findings of COVID-19 associated with acute respiratory distress syndrome. The Lancet Respiratory Medicine *8*, 420-422.

Yan, B., Chu, H., Yang, D., Sze, K.-H., Lai, P.-M., Yuan, S., Shuai, H., Wang, Y., Kao, R.Y.-T., Chan, J.F.-W., *et al.* (2019a). Characterization of the Lipidomic Profile of Human

Coronavirus-Infected Cells: Implications for Lipid Metabolism Remodeling upon Coronavirus Replication. Viruses *11*, 73.

Yan, B., Chu, H., Yang, D., Sze, K.H., Lai, P.M., Yuan, S., Shuai, H., Wang, Y., Kao, R.Y., Chan, J.F., *et al.* (2019b). Characterization of the Lipidomic Profile of Human Coronavirus-Infected Cells: Implications for Lipid Metabolism Remodeling upon Coronavirus Replication. Viruses *11*.

Yang, J.K., Lin, S.S., Ji, X.J., and Guo, L.M. (2010). Binding of SARS coronavirus to its receptor damages islets and causes acute diabetes. Acta Diabetol *47*, 193-199.

Yoshizumi, T., Ichinohe, T., Sasaki, O., Otera, H., Kawabata, S.-i., Mihara, K., and Koshiba, T. (2014). Influenza A virus protein PB1-F2 translocates into mitochondria via Tom40 channels and impairs innate immunity. Nature Communications *5*, 4713.

Yuan, S., Chu, H., Chan, J.F.-W., Ye, Z.-W., Wen, L., Yan, B., Lai, P.-M., Tee, K.-M., Huang, J., Chen, D., *et al.* (2019). SREBP-dependent lipidomic reprogramming as a broad-spectrum antiviral target. Nature Communications *10*, 120.

Zhao, J., Tian, M., Zhang, S., Delfarah, A., Gao, R., Rao, Y., Savas, A.C., Lu, A., Bubb, L., Lei, X., *et al.* (2020). Deamidation Shunts RelA from Mediating Inflammation to Aerobic Glycolysis. Cell Metabolism *31*, 937-955.e937.

Zhu, L., She, Z.-G., Cheng, X., Qin, J.-J., Zhang, X.-J., Cai, J., Lei, F., Wang, H., Xie, J., Wang, W., *et al.* (2020). Association of Blood Glucose Control and Outcomes in Patients with COVID-19 and Pre-existing Type 2 Diabetes. Cell Metabolism.

Supplementary Information

Table S1. Differentially expressed genes in response to SARS-CoV-2 infection by RNA-seq of primary bronchial epithelial cell cultures and COVID-19 patient biopsies

Table S2. Gene list of the assembled metabolic categories

Table S3. Summary of Transcription Factor Targets Genes in Lipid Metabolism

Table S4. Summary of Transcription Factor Targets Genes in Mitochondria

Table S5. Summary of Transcription Factor Targets Genes in Glucose Metabolism

Figure S1. Endoplasmic stress and lipid accumulation. (**A**) Schematic depicting ER stress pathways superimposed with pathway-associated genes from SARS-CoV-2 infected lung cells and COVID-19 patient biopsies. Red and green boxes are up and downregulated by infection, respectively. * marks differentially regulated genes (n=3, FDR<0.05). Red and green arrows schematically note interactions based on the transcriptional response. XBP1S is the IRE1 spliced form of XBP1. (**B**) Schematic of pathway-specific interactions between viral proteins (black), host protein (green), and the main genes in the ATF6 ER stress pathway (blue). SPP1 appears to physically interact with numerous viral proteins. (**C**) Schematic of lipid metabolism fluxes. Lipid metabolism genes changed by SARS-CoV-2 infection are superimposed, marked red, and green for up and downregulation, respectively. * marks differentially regulated genes (n=3, FDR <0.01).

Figure S2. Mitochondrial stress and glucose metabolism. (**A**) Schematic of citric acid cycle fluxes. Citric acid cycle genes changed by SARS-CoV-2 infection superimposed, marked red, and green for up and downregulation, respectively. * marks differentially regulated genes (n=3, FDR <0.01). (**B**) Expanded schematic of possible interactions between viral proteins (black), host protein (green), and enzymes controlling the citric acid cycle. (**C**) Schematic of glucose metabolism fluxes. Glucose metabolism genes changed by SARS-CoV-2 infection are superimposed, marked red, and green for up and downregulation, respectively. * marks differentially regulated genes (n=3, FDR <0.01).

Figure S3. The response of SARS-CoV-2 Infected Lung Cells to Metabolic Regulators. Viability of SARS-CoV-2 infected primary lung epithelial cells exposed to various drugs or vehicle control (*methods*) for 5 days. Post-treatment was assessed by Hoechst 33258 staining and normalized to vehicle control (blue bars). Treatment with 10 μM GW992 reduced cell viability by 50% ($p<0.01$).

SARS-CoV-2 viral load was similarly quantified on day 5 of treatment (*methods*). Treatment with 20 μM fenofibrate reduced SARS-CoV-2 viral load by 1.9-logs close to the detection limit of the assay (n=3; $p<0.001$). Treatment with 10 μM GW992 or 10 μM cloperastine reduced viral load by 2.5 to 3-fold, respectively (n=3; $p<0.05$).

Figure 1

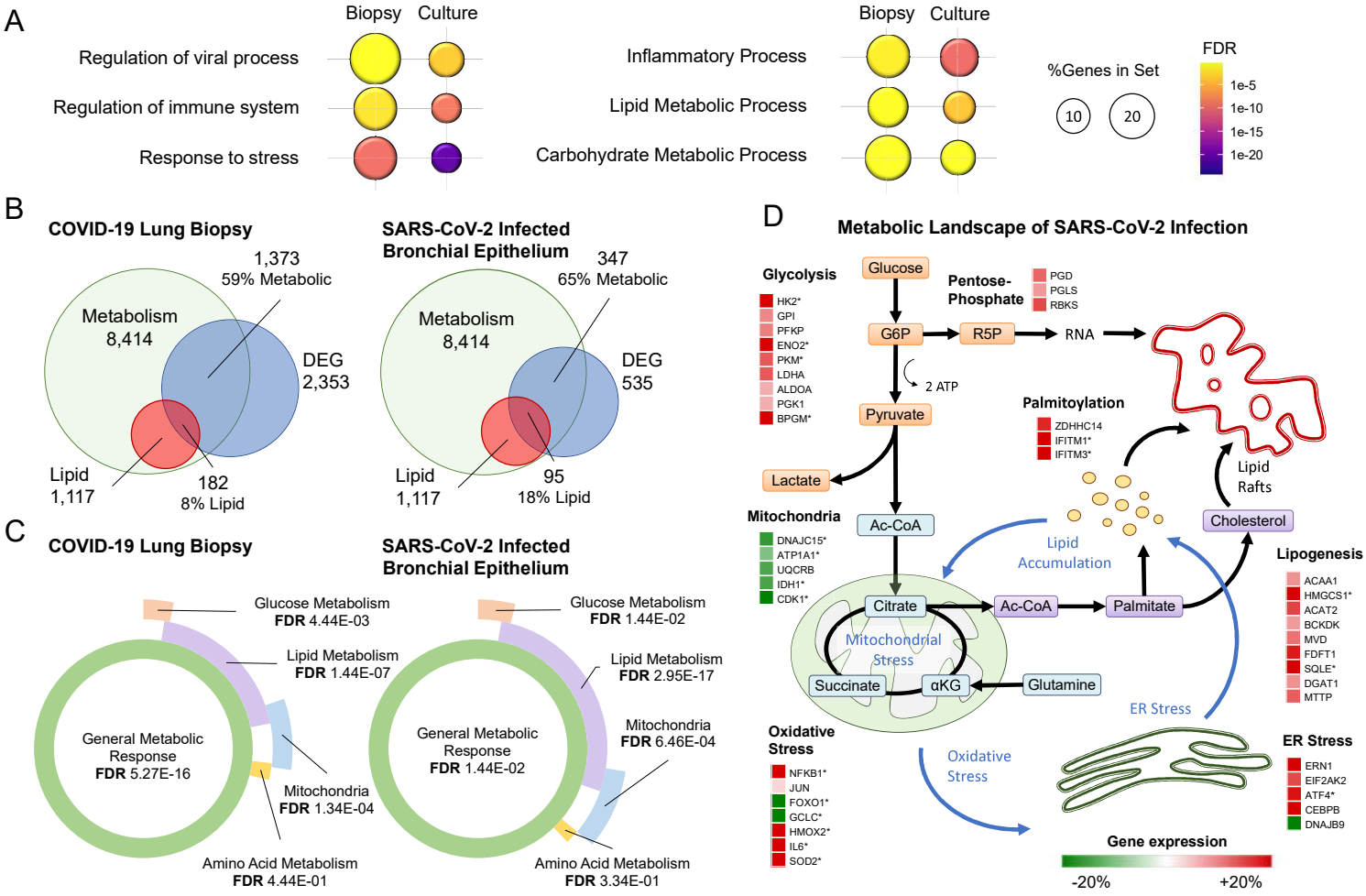

Figure 2

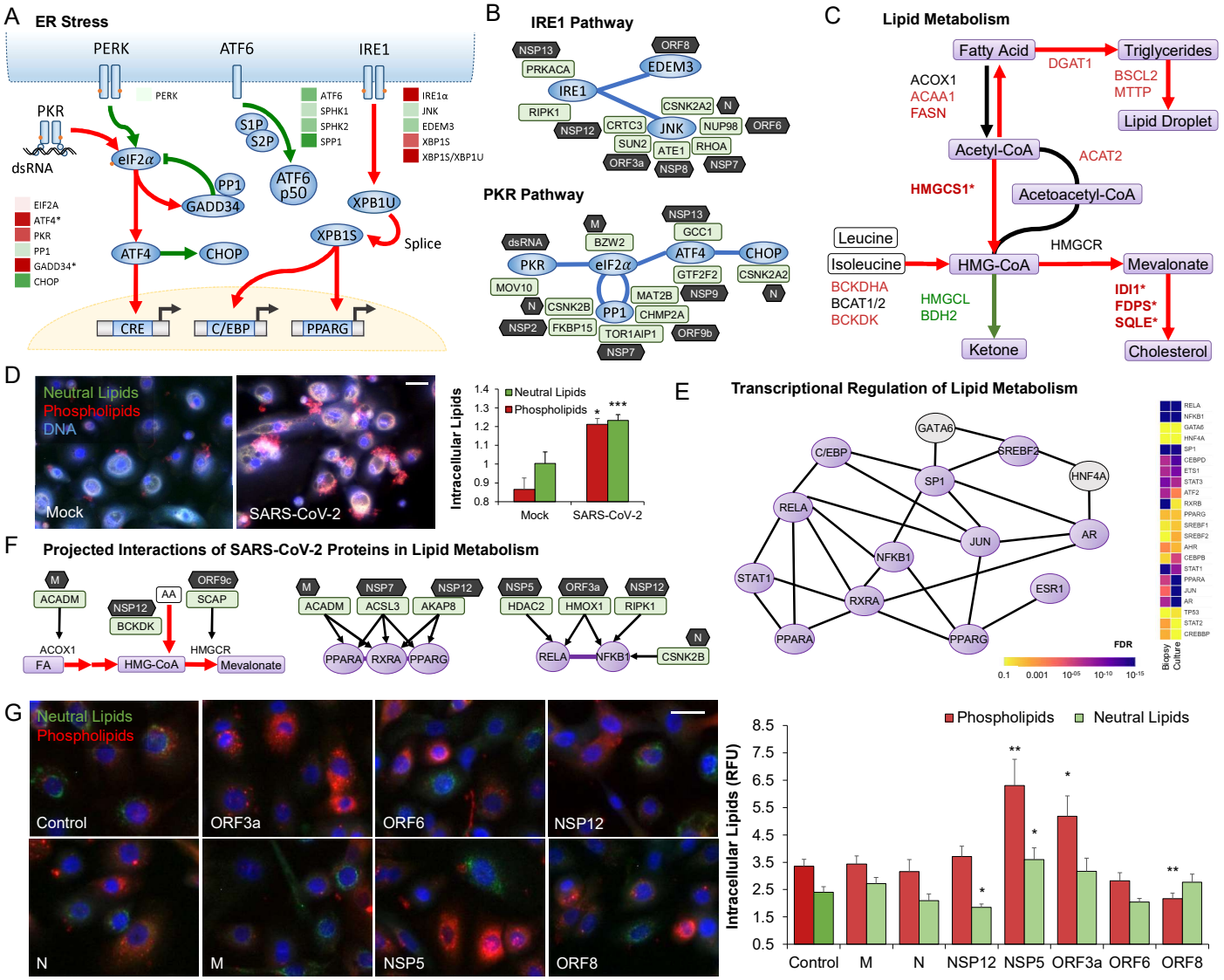

Figure 3

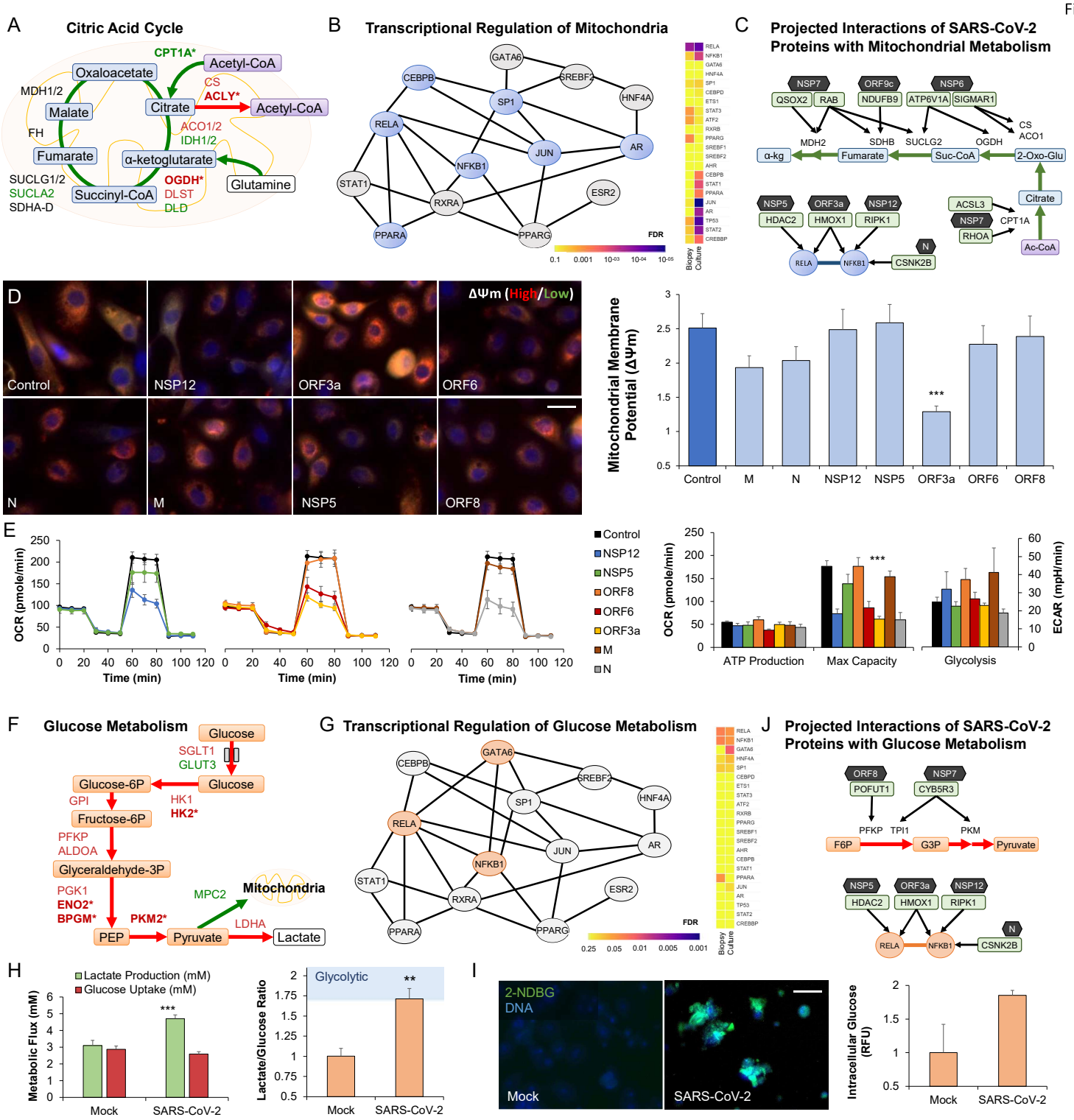

Figure 4

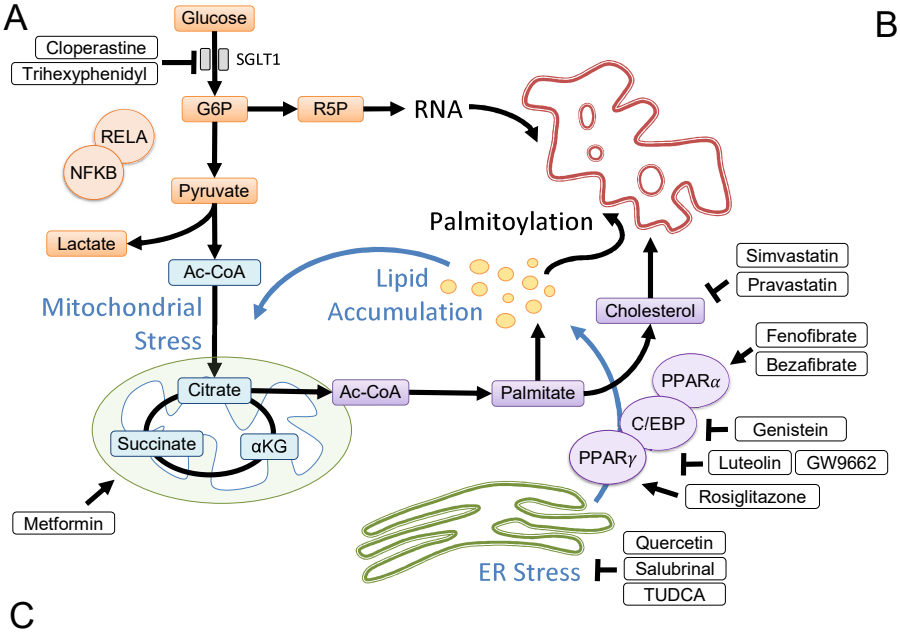

B

	Drug Name	Indication	Therapeutic Target
Glycolysis	Cloperastine (Hustazol®)	Cough Suppressant	SGLTI/II inhibitor
	Trihexyphenidyl (Artane®)	Parkinson's Disease	SGLTI/II inhibitor
	Metformin (Fortamet®)	Type II Diabetes	AMPK activator
Lipid Metabolism	Simvastatin (Zocor®)	Dyslipidemia	HMGCR inhibitor
	Pravastatin (Pravachol®)	Dyslipidemia	HMGCR inhibitor
	Fenofibrate (Fenoglide®)	Dyslipidemia	PPARα agonist
	Bezafibrate (Bezalip®)	Dyslipidemia	PPARα agonist
	Genistein (isoflavone)	Dietary supplement	C/EBP inhibitor
	Luteolin (flavone)	Dietary supplement	PPARγ inhibitor
	Imatinib (Gleevec®)	Cancer	PPARγ inhibitor
ER Stress	Quercetin (flavonoid)	Dietary supplement	IRE1α inhibitor
	Salubrinal		eIF2α inhibitor
	TUDCA (bile acid)	Chinese medicine	PERK inhibitor
	UDCA (Actigall®)	Cholelithiasis	CHOP activator

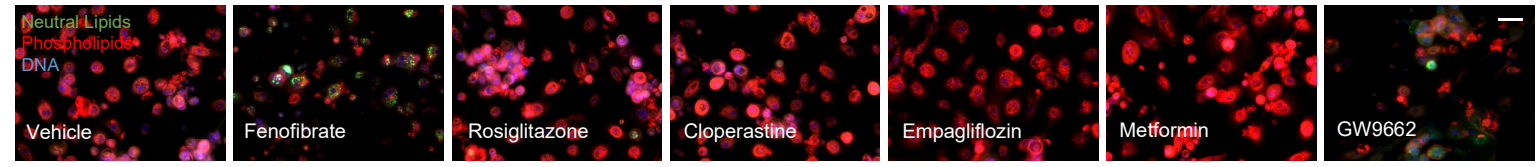

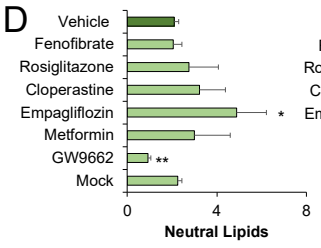

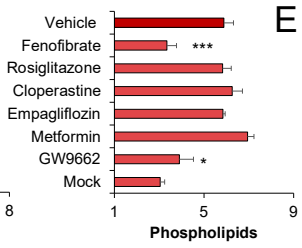

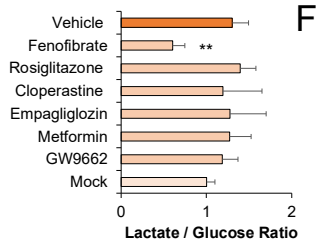

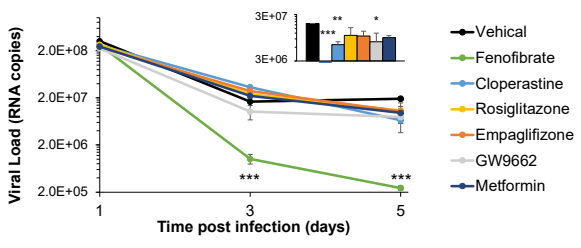

Figure S1

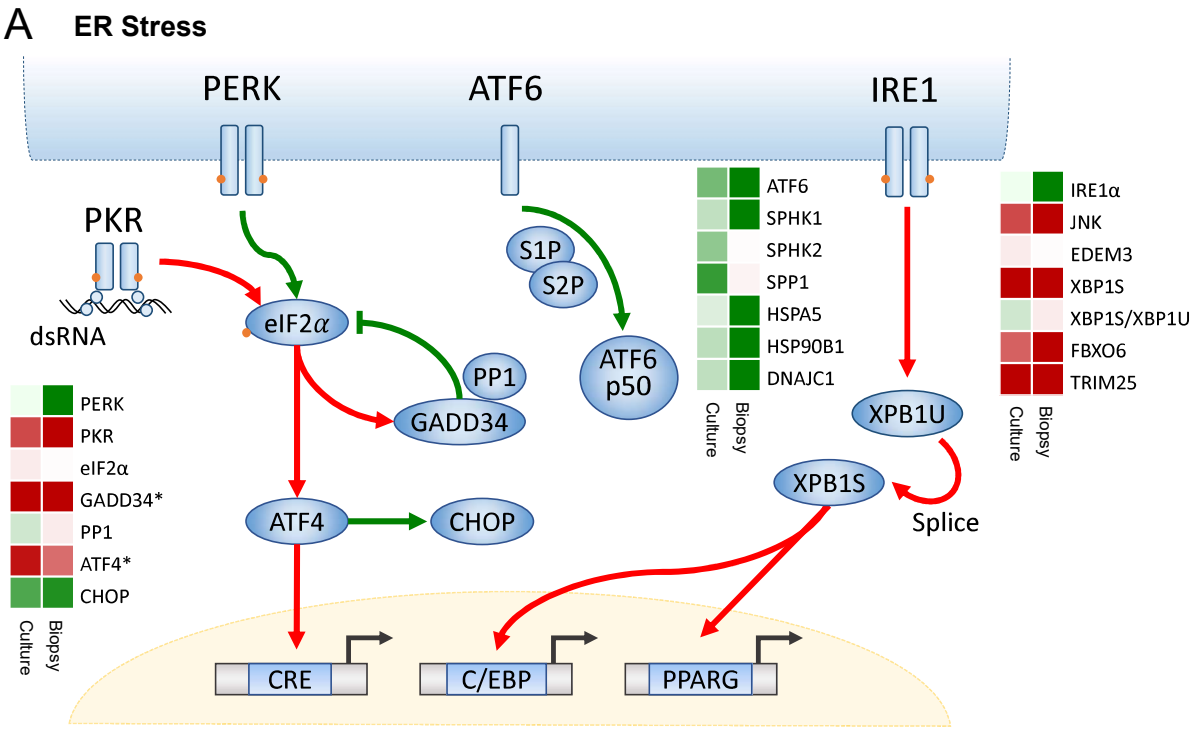

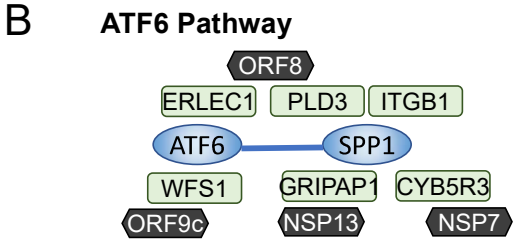

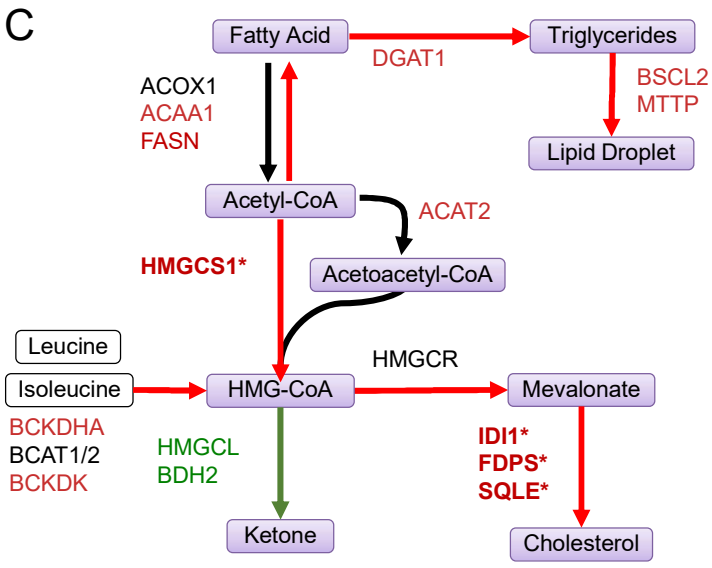

Lipid Metabolism

Gene Expression			
ACOX1		BCAT2	
FASN		BCKDK	
ACACA		HMGCL	
ACAA1		BDH2	
DGAT1		HMGCR	
ACAT2		MVK	
BSCL2		MVD	
MTTP		IDI1*	
HMGCS1*		FDPS*	
BCKDHA		SQLE*	

-20% +20%

Figure S2

A

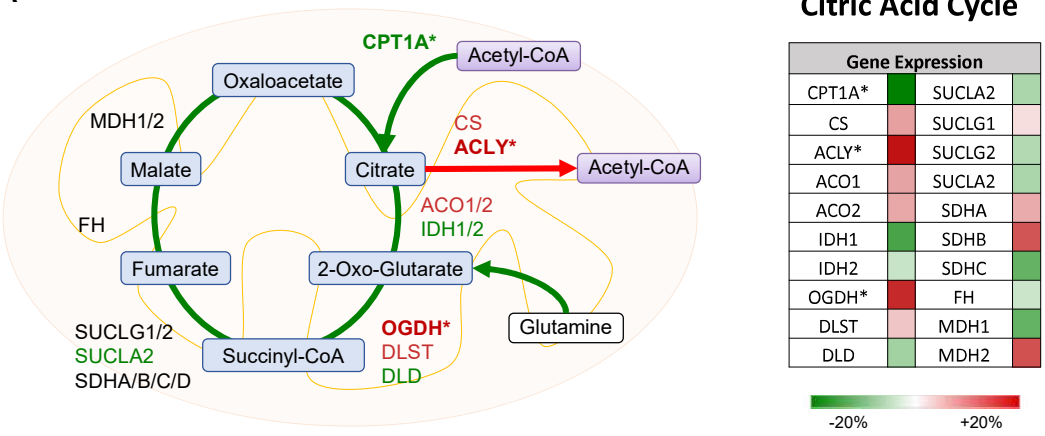

Citric Acid Cycle

Gene Expression			
CPT1A*		SUCLA2	
CS		SUCLG1	
ACLY*		SUCLG2	
ACO1		SUCLA2	
ACO2		SDHA	
IDH1		SDHB	
IDH2		SDHC	
OGDH*		FH	
DLST		MDH1	
DLD		MDH2	

-20% +20%

B

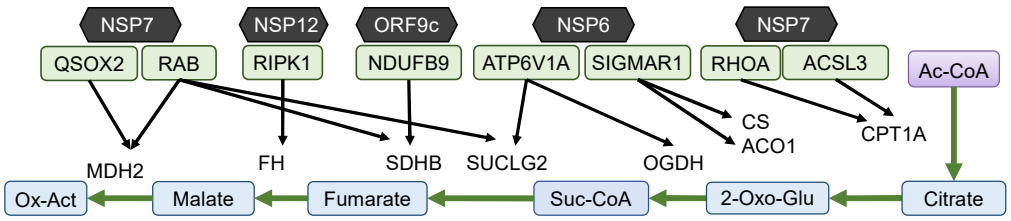

C

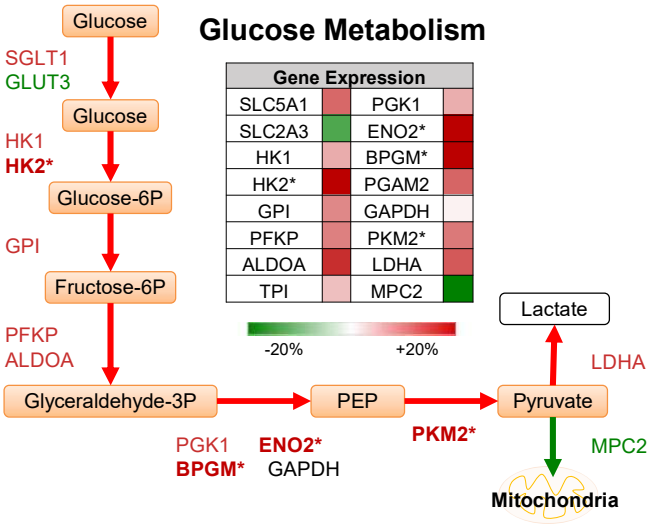

Glucose Metabolism

Gene Expression			
SLC5A1		PGK1	
SLC2A3		ENO2*	
HK1		BPGM*	
HK2*		PGAM2	
GPI		GAPDH	
PFKP		PKM2*	
ALDOA		LDHA	
TPI		MPC2	

-20% +20%

Figure S3